

# Lawrence Berkeley National Laboratory

## LBL Publications

### Title

Producing circular field harmonics inside elliptic magnet apertures with superconducting canted-cosine-theta coils

### Permalink

<https://escholarship.org/uc/item/7r53684w>

### Journal

Physical Review Accelerators and Beams, 27(2)

### ISSN

1098-4402

### Author

Brouwer, L

### Publication Date

2024-02-01

### DOI

10.1103/physrevaccelbeams.27.022402

### Copyright Information

This work is made available under the terms of a Creative Commons Attribution License, available at <https://creativecommons.org/licenses/by/4.0/>

Peer reviewed

## Producing circular field harmonics inside elliptic magnet apertures with superconducting canted-cosine-theta coils

L. Brouwer<sup>\*</sup>

*Accelerator Technology and Applied Physics Division, Lawrence Berkeley National Laboratory, Berkeley, California 94720, USA*



(Received 8 January 2024; accepted 12 February 2024; published 27 February 2024)

Superconducting magnets with noncircular aperture are desired for accelerators and many other high-field applications. This paper presents new methods for the analytic design of elliptic bore superconducting accelerator magnets. Part 1 of this work shares the derivation of current to field relations between a sheet current density on an elliptic cylinder and the magnetic field harmonics inside the aperture. This result is explored in the general context of elliptic bore magnet design with relevant scaling laws compared between elliptic and circular bore magnets. In part 2, this approach is applied to the specific geometry of canted-cosine-theta (CCT) accelerator magnets, enabling analytic winding design for single or mixed circular harmonics within elliptic aperture CCT magnets.

DOI: [10.1103/PhysRevAccelBeams.27.022402](https://doi.org/10.1103/PhysRevAccelBeams.27.022402)

### I. INTRODUCTION

High field magnets with noncircular apertures are advantageous for a wide range of accelerator applications. In fixed-field accelerators, the energy-dependent orbit excursion typically leads to the beam sampling of a larger region in the horizontal plane [1,2]. A similar effect of orbit offset between circulating and extracted beams in some rapid-cycling synchrotrons also motivates the use of elliptic bore magnets [3]. Furthermore, noncircular apertures allow for the efficient passing of multiple beams through a single magnet in collider interaction regions. In addition to multiorbit motivations, there are applications like heavy ion synchrotrons, where an elliptic bore magnet is a better match to the beam shape [4,5].

There are economic and technical motivations for choosing an elliptic aperture when this shape matches the beam-prescribed field region. The smaller bore area when compared to a circular aperture leads to a reduction in stored energy and coil volume, both of which are magnet cost drivers. In addition, if the magnet poles reside only on the minor axis (e.g., dipoles with a larger horizontal aperture), the effective aperture reduction to the pole results in shorter coil ends and magnet physical length for the same integrated field. The corresponding reduction in magnet size along the minor axis may also benefit designs in space-constrained areas near collider interaction regions

or within detectors. Finally, elliptic apertures allow for the efficient integration of in-bore radiation shielding concentrated at the midplane, a potential benefit for muon colliders and other future accelerators with high radiation loads in the horizontal plane [6,7].

Elliptic bore accelerator magnets are rare, and even more so for fields greater than 2–3 T, where superconducting windings rather than ferromagnetic material dominate field production. In the 4–5 T range, there are published design studies of elliptic aperture Nb-Ti magnets for fixed-field accelerators [8] and for a future medical synchrotron at National Institutes for Quantum and Radiological Science and Technology in Japan [9]. The project team there recently tested a prototype combined function magnet with an elliptic aperture that successfully reached the design field of 4.5 T at the windings [10]. For field levels beyond the limits of Nb-Ti, there is an initial study of elliptic aperture Nb<sub>3</sub>Sn magnets for the muon collider [6] as well as several rectangular bore Nb<sub>3</sub>Sn magnet designs for testing superconducting cables in background fields up to 15 T [11–13]. While not explicitly for use in accelerators, these 15 T superconducting magnets share many features that make them highly relevant to accelerator dipoles with slightly noncircular aperture.

While field quality in elliptic apertures has been studied in detail [14,15], to the best of our knowledge, an analytic approach to the electromagnetic design of elliptic bore superconducting accelerator magnets is missing from published literature. We seek to address this need by sharing an analytic design method that is generally relevant to elliptically shaped superconducting windings and then applying it to the specific geometry of canted-cosine-theta (CCT) magnet design. The CCT design, which was first published in 1970 [16], has experienced a growing interest

\*lbrouwer@lbl.gov

*Published by the American Physical Society under the terms of the Creative Commons Attribution 4.0 International license. Further distribution of this work must maintain attribution to the author(s) and the published article's title, journal citation, and DOI.*

over the last 20 years for potential advantages of conductor stress management, simplified manufacturing for small series of magnets, and natural ability to produce single or combined function fields of accelerator quality [17,18].

The continuation of this paper is organized as follows: Section II first introduces elliptic coordinates and field harmonics and then derives the relation between current density on an elliptic boundary and circular harmonics within the aperture. Section III employs these relations to study the tradeoffs between circular and elliptic windings by deriving scaling laws for magnet cost drivers as a function of winding ellipticity. This general framework is then applied to analytic coil design of CCT magnets in Sec. IV. Finally, discussion and conclusions are shared in Sec. V.

## II. CURRENT TO FIELD RELATIONS FOR AN ELLIPTIC CURRENT SHEET

### A. Elliptic cylindrical coordinates

Figure 1 shows the elliptic cylindrical coordinate system formed by constant coordinate surfaces of confocal cylinders and planes. This system is advantageous for the analytic design of elliptic bore superconducting magnets since boundary conditions from elliptic aperture windings can be applied to general solutions of Laplace's equation on a constant coordinate surface.

In the notation of Moon and Spencer [19], the elliptic cylindrical coordinates are

$$\begin{aligned} u^1 &= \eta, & 0 \leq \eta < \infty, \\ u^2 &= \psi, & 0 \leq \psi < 2\pi, \\ u^3 &= z, & -\infty < z < \infty, \end{aligned} \quad (1)$$

which can be related to Cartesian coordinates through  $x = a \cosh \eta \cos \psi$ ,  $y = a \sinh \eta \sin \psi$ , and  $z = z$ , with scale factors of

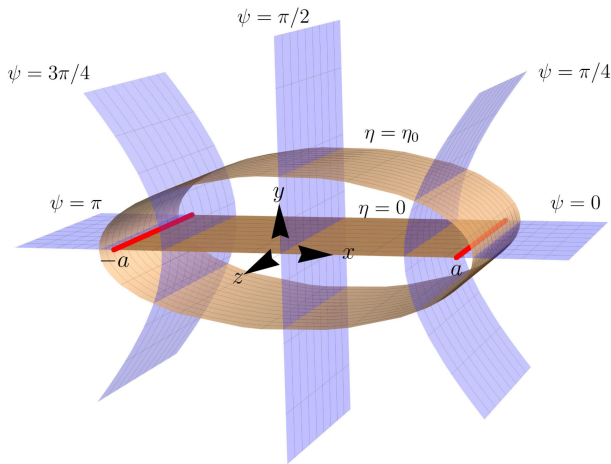


FIG. 1. Constant  $\eta$  and  $\psi$  surfaces for the elliptic coordinates form confocal cylinders and planes.

$$\begin{aligned} h_1 &= h_2 = a \sqrt{\cosh^2 \eta - \cos^2 \psi}, \\ h_3 &= 1. \end{aligned} \quad (2)$$

Critically for elliptic bore magnets, the constant  $\eta = \eta_0$  surface

$$\left( \frac{x}{a \cosh \eta_0} \right)^2 + \left( \frac{y}{a \sinh \eta_0} \right)^2 = 1 \quad (3)$$

forms a confocal cylinder that can be matched to the superconducting windings and thus also the surface on which the magnetic boundary conditions are evaluated.

### B. Magnetic vector potential and field harmonics in elliptic coordinates

We look to find a magnetic vector potential  $\mathbf{A}$  in elliptic coordinates from which the corresponding elliptic field harmonics are given by  $\mathbf{B} = \nabla \times \mathbf{A}$ . Considering Maxwell's equations for source free regions,  $\nabla \times \mathbf{B} = \nabla \times (\nabla \times \mathbf{A}) = 0$ , and assuming no axial variation such that  $\mathbf{A} = A_z(\eta, \psi) \hat{z}$ , the potential equation to be solved takes the form of the vector Laplacian  $\nabla^2 \mathbf{A} = 0$ . We apply our assumptions and the scale factors in Eq. (2) to the general vector Laplacian for curvilinear coordinates in [20] to find the resulting potential equation

$$\nabla^2 \mathbf{A} = \frac{1}{a^2 (\cosh^2 \eta - \cos^2 \psi)} \left( \frac{\partial^2 A_z}{\partial \eta^2} + \frac{\partial^2 A_z}{\partial \psi^2} \right) = 0. \quad (4)$$

The general solution of this equation is well known and can be expressed as a mix of

$$\begin{aligned} A_z &= A_n \cosh(n\eta) \cos(n\psi) + B_n \cosh(n\eta) \sin(n\psi) \\ &+ C_n \sinh(n\eta) \cos(n\psi) + D_n \sinh(n\eta) \sin(n\psi), \end{aligned} \quad (5)$$

and

$$\begin{aligned} A_z &= E_n e^{-n\eta} \cos(n\psi) + F_n e^{-n\eta} \sin(n\psi) \\ &+ G_n e^{n\eta} \cos(n\psi) + H_n e^{n\eta} \sin(n\psi), \end{aligned} \quad (6)$$

with an implied summation over  $n$ . Next, we select terms from this general solution for regions inside and outside an elliptic boundary of  $\eta = \eta_0$  considering the limiting behavior at  $\eta \rightarrow 0$  and  $\eta \rightarrow \infty$ . For brevity, we make an additional selection of terms in the bore producing the midplane symmetry  $\mathbf{B}(\eta = 0) \cdot \hat{\psi} = 0$  to maintain upright, nonskew field harmonics (since the derivation of the skew terms can be found with the assumption of opposite symmetry and the same methodology to follow). With these conditions, the vector potential inside and outside of the elliptic boundary is

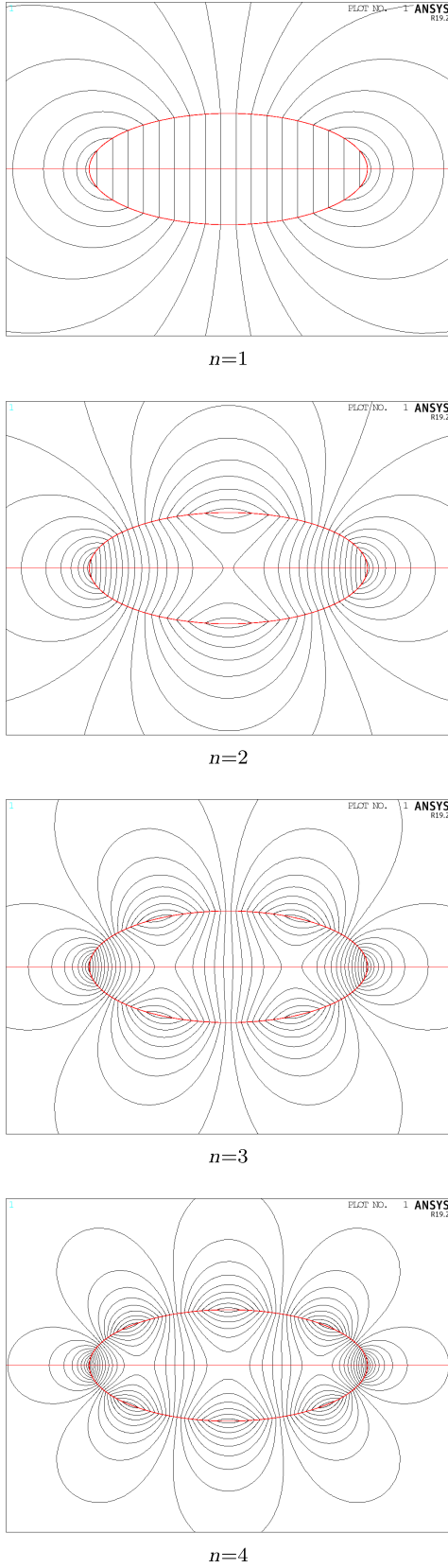


FIG. 2. The first four elliptic field harmonics for an example elliptic boundary.

$$\mathbf{A}(\eta, \psi) = \begin{cases} A_n^{\text{in}} \cosh(n\eta) \cos(n\psi) \hat{z}, & \eta < \eta_0 \\ A_n^{\text{out}} e^{-n\eta} \cos(n\psi) \hat{z}, & \eta > \eta_0 \end{cases}. \quad (7)$$

We use  $\mathbf{B} = \nabla \times \mathbf{A}$  to derive the magnetic field harmonics  $\mathbf{B} = B_\eta \hat{\eta} + B_\psi \hat{\psi}$  from this potential, resulting in

$$B_\eta(\eta, \psi) = \begin{cases} -\frac{nA_n^{\text{in}} \cosh(n\eta) \sin(n\psi)}{a \sqrt{\cosh^2 \eta - \cos^2 \psi}}, & \eta < \eta_0 \\ -\frac{nA_n^{\text{out}} e^{-n\eta} \sin(n\psi)}{a \sqrt{\cosh^2 \eta - \cos^2 \psi}}, & \eta > \eta_0 \end{cases}, \quad (8)$$

and

$$B_\psi(\eta, \psi) = \begin{cases} -\frac{nA_n^{\text{in}} \sinh(n\eta) \cos(n\psi)}{a \sqrt{\cosh^2 \eta - \cos^2 \psi}}, & \eta < \eta_0 \\ \frac{nA_n^{\text{out}} e^{-n\eta} \cos(n\psi)}{a \sqrt{\cosh^2 \eta - \cos^2 \psi}}, & \eta > \eta_0 \end{cases}. \quad (9)$$

Figure 2 shows the first four elliptic harmonics in Eqs. (8) and (9) evaluated for the example boundary  $\eta_0 = \tanh^{-1}(10/25)$  using the commercial software ANSYS. Deviation from the circular harmonics typically used for accelerator design starts at  $n = 3$  (the sextupolelike term), where among other differences, a clear splitting of the zero field location begins. In Sec. II D, we will derive relations between elliptic and circular harmonics to find the combination of elliptic field harmonics required to “correct” the deviation of  $n \geq 3$  harmonics and produce single or combined function circular harmonics in an elliptic aperture.

### C. Elliptic harmonics related to an elliptic current sheet density

We relate the elliptic harmonics to an axial current sheet at the boundary, deriving an idealized current density to be approximated by discrete coil design. The magnetic boundary conditions at the  $\eta = \eta_0$  surface of an elliptic cylinder require

$$(B_\eta^{\text{out}} - B_\eta^{\text{in}})|_{\eta=\eta_0} = 0, \quad (10)$$

and

$$(B_\psi^{\text{out}} - B_\psi^{\text{in}})|_{\eta=\eta_0} = \mu_0 j_z, \quad (11)$$

where  $\mathbf{j} = j_z \hat{z}$  is the sheet current density on the surface. We apply the condition in Eq. (11) to the field harmonics in Eqs. (8) and (9) to define the general form of the current density as

$$j_z(\psi) = \frac{j_{0nz} \cos(n\psi)}{\sqrt{\cosh^2 \eta_0 - \cos^2 \psi}}, \quad (12)$$

where summation over  $n$  is implied and  $j_{0nz}$  is constant. We then apply both boundary conditions to relate the

vector potential and field harmonics to the current density through

$$\mathbf{A}(\eta, \psi) = \begin{cases} \frac{\mu_0 j_{0nz} a e^{-n\eta_0} \cosh(n\eta) \cos(n\psi)}{n} \hat{\mathbf{z}}, & \eta < \eta_0 \\ \frac{\mu_0 j_{0nz} a \cosh(n\eta_0) e^{-n\eta} \cos(n\psi)}{n} \hat{\mathbf{z}}, & \eta > \eta_0 \end{cases}, \quad (13)$$

$$B_\eta(\eta, \psi) = \begin{cases} -\frac{\mu_0 j_{0nz} e^{-n\eta_0} \cosh(n\eta) \sin(n\psi)}{\sqrt{\cosh^2 \eta - \cos^2 \psi}}, & \eta < \eta_0 \\ -\frac{\mu_0 j_{0nz} \cosh(n\eta_0) e^{-n\eta} \sin(n\psi)}{\sqrt{\cosh^2 \eta - \cos^2 \psi}}, & \eta > \eta_0 \end{cases}, \quad (14)$$

and

$$B_\psi(\eta, \psi) = \begin{cases} -\frac{\mu_0 j_{0nz} e^{-n\eta_0} \sinh(n\eta) \cos(n\psi)}{\sqrt{\cosh^2 \eta - \cos^2 \psi}}, & \eta < \eta_0 \\ \frac{\mu_0 j_{0nz} \cosh(n\eta_0) e^{-n\eta} \cos(n\psi)}{\sqrt{\cosh^2 \eta - \cos^2 \psi}}, & \eta > \eta_0 \end{cases}, \quad (15)$$

which prescribes the current density required to produce single or combined function elliptic harmonics in an elliptic aperture.

#### D. Circular harmonics related to an elliptic current sheet density

Accelerator design and beam dynamics codes typically describe magnetic fields in terms of circular harmonics (leading to the traditional definition of dipole, quadrupole, sextupole, and higher order magnets). For this reason, we take the next step beyond Sec. II C and relate an elliptically shaped current density to circular harmonics within the aperture. We can derive the circular harmonics using the

same vector potential method in Sec. II B with cylindrical coordinates, but because these are so well known, we simply restate the relevant harmonics

$$\mathbf{B}(r, \theta) = -\frac{\mu_0 j_{0nz}}{2} \left(\frac{r}{r_0}\right)^{n-1} (\sin n\theta \hat{\mathbf{r}} + \cos n\theta \hat{\boldsymbol{\theta}}) \quad (16)$$

within a circular aperture of radius  $r_0$  carrying a sheet current density  $\mathbf{j} = j_{0nz} \cos(n\theta) \hat{\mathbf{z}}$ . We define normalized field coefficients  $B_n = B/r^{n-1}$  so that  $B_1$  is the dipole field (e.g., T),  $B_2$  is the quadrupole gradient (e.g., T/m),  $B_3$  is the sextupole component (e.g., T/m<sup>2</sup>), and so forth. The relationship between the current and field coefficients for the circular harmonics is then

$$j_{0nz} = -\frac{2B_n}{\mu_0} r_0^{n-1}. \quad (17)$$

To relate the circular field harmonics to an elliptic current density, we define the matrices  $\mathbf{T}_{mk}$  and  $\mathbf{E}_{kn}$  as

$$\mathbf{j}_{0n} = (\mathbf{E}_{kn})(\mathbf{T}_{mk})^{-1} \mathbf{B}_{0n}, \quad (18)$$

where  $\mathbf{j}_{0n} = (j_{01z}, j_{02z}, \dots, j_{0nz})$  is the elliptic current density coefficient vector for Eq. (12) and  $\mathbf{B}_{0n} = (B_1, B_2, \dots, B_n)$  is a vector of desired circular field harmonics which may be single or combined function. We chose this form to build on the published work of Schnizer focused on relating circular and elliptic harmonics for magnetic measurement techniques [14]. From this reference, the  $\mathbf{T}_{mk}$  matrix (which relates 2D elliptic and cylindrical field harmonics without approximation) is

$$\mathbf{T}_{mk} = \frac{1}{(1 + \delta_{k,0}) \cosh(k\eta_0) a^m} \begin{cases} \frac{(-1)^{m/2} \cos(k\pi/2)}{m!} \prod_{\mu=1}^{m/2} (k^2 - [2(\mu-1)]^2) & m \text{ is even} \\ \frac{(-1)^{(m-1)/2} \sin(k\pi/2) k}{m!} \prod_{\mu=1}^{(m-1)/2} (k^2 - (2\mu-1)^2) & m \text{ is odd} \end{cases}, \quad (19)$$

where  $m$  is the matrix row and  $k$  is the column (with indices starting at zero). The second, new matrix  $\mathbf{E}_{kn}$  relates the elliptic harmonics to elliptic current density coefficients by reformatting the results derived in Sec. II C. Considering the already defined form of  $\mathbf{T}_{mk}$ ,

$$\mathbf{E}_{kn} = -\frac{e^{k\eta_0}}{2\mu_0} \left( \frac{\delta_{k,n}}{\cosh((k-1)\eta_0)} - \frac{\delta_{k,n-2}}{\cosh((k+1)\eta_0)} \right), \quad (20)$$

where  $k$  is the matrix row and  $n$  is the column (with indices starting at one). In practice, these matrices can be truncated up to some order of the desired  $n$ th harmonic contribution.

Table I lists the evaluation of Eq. (18) for the first four circular harmonics (due to their importance in accelerator design). For the dipole and quadrupole, only a magnitude

scaling of the matching current density term is required to convert elliptic to circular harmonics. Starting with the sextupole at  $n=3$ , an additional  $n-2$  elliptic current density term is needed, indicating that a combination of

TABLE I. Elliptic current density coefficients  $j_{0nz}$  [in Eq. (12)] for producing the circular harmonics  $B_n$ .

	$j_{01z}$	$j_{02z}$	$j_{03z}$	$j_{04z}$
$B_1$	$-\frac{B_1 e^{\eta_0}}{\mu_0}$			
$B_2$		$-a \frac{B_2 e^{2\eta_0}}{2\mu_0}$		
$B_3$	$-a^2 \frac{B_3 e^{\eta_0}}{4\mu_0}$		$-a^2 \frac{B_3 e^{3\eta_0}}{4\mu_0}$	
$B_4$		$-a^3 \frac{B_4 e^{2\eta_0}}{4\mu_0}$		$-a^3 \frac{B_4 e^{4\eta_0}}{8\mu_0}$

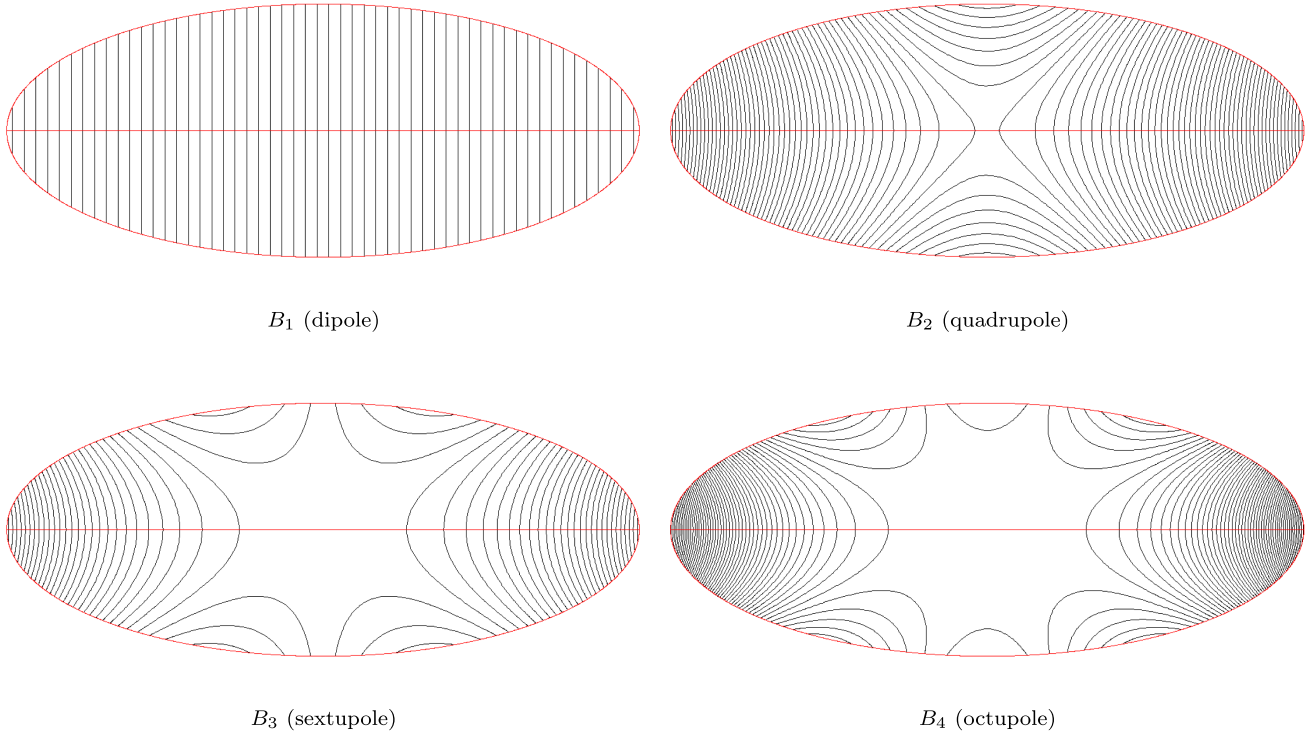


FIG. 3. The current densities in Table I are applied to produce the first four circular field harmonics inside an example elliptic aperture.

elliptic harmonics is required to produce  $n \geq 3$  circular harmonics. Ultimately, this method allows us to determine the continuous current density on an elliptic cylinder required to produce single or combined function circular harmonics in the aperture.

Figure 3 shows results from an ANSYS model implementing the current density coefficients in Table I for an example elliptic bore of  $\eta_0 = \tanh^{-1}(10/25)$ . We clearly see the “correction” of the  $n \geq 3$  harmonics when compared to the elliptic harmonics for the same geometry in Fig. 2.

### III. COMPARISON OF SCALING LAWS BETWEEN ELLIPTIC AND CIRCULAR APERTURES

For applications where beam dynamics prescribes an elliptic region of the field, we must choose between a circular bore sized to the maximum beam aperture or an elliptic bore better matched to the space required for the beam (illustrated in Fig. 4). To quantify this trade-off, we derive the cost drivers [21] of stored energy and conductor use as a function of aperture ellipticity

$$\epsilon = 1 - \frac{b_y}{a_x}, \quad (21)$$

where  $a_x$  and  $b_y$  are the major and minor axes of the windings.

To find the magnetic stored energy, we use the integral approach  $E = \frac{1}{2} \int (\mathbf{A} \cdot \mathbf{J}) dV$ . With the assumptions we made for the vector potential and current density in the previous sections, this reduces to a stored energy per length of

$$E_{ell} = \frac{a}{2} \int (\mathbf{A} \cdot \mathbf{j}) \sqrt{\cosh^2 \eta_0 - \cos^2 \psi} d\psi, \quad (22)$$

for an elliptic current sheet at  $\eta = \eta_0$ , and

$$E_{cyl} = \frac{r_0}{2} \int (\mathbf{A} \cdot \mathbf{j}) d\theta, \quad (23)$$

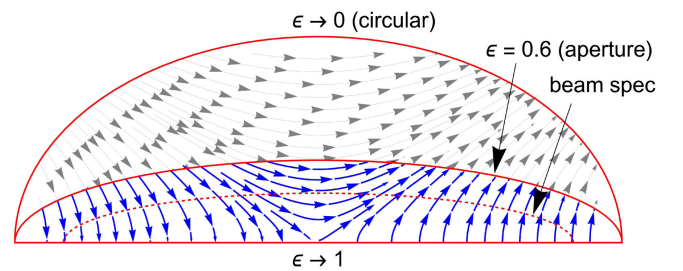


FIG. 4. An example choice between a circular or elliptic bore quadrupole magnet with matched major axis. We use comparisons of this type to quantify the advantages of elliptic bore magnets.

TABLE II. Stored energy and amp turns for elliptic and circular sheets producing the same circular harmonics.

	$E_{\text{ell}}$	$At_{\text{ell}}$	$E_{\text{cyl}}$	$At_{\text{cyl}}$	$E_{\text{ell}}/E_{\text{cyl}}$	$At_{\text{ell}}/At_{\text{cyl}}$
$B_1$	$\frac{\pi a^2 B_1^2}{2\mu_0} e^{\eta_0} \cosh(\eta_0)$	$\frac{4a B_1 }{\mu_0} e^{\eta_0}$	$\frac{\pi B_1^2}{\mu_0} r_0^2$	$8 \frac{ B_1 }{\mu_0} r_0$	$1 - \frac{\epsilon}{2}$	$1 - \frac{\epsilon}{2}$
$B_2$	$\frac{\pi a^4 B_2^2}{16\mu_0} e^{2\eta_0} \cosh(2\eta_0)$	$\frac{2a^2 B_2 }{\mu_0} e^{2\eta_0}$	$\frac{\pi B_2^2}{2\mu_0} r_0^4$	$8 \frac{ B_2 }{\mu_0} r_0^2$	$1 - 2\epsilon + \frac{7\epsilon^2}{4} - \frac{3\epsilon^3}{4} + \frac{\epsilon^4}{8}$	$1 - \epsilon + \frac{\epsilon^2}{4}$

for a circular current sheet at radius  $r = r_0$ . To find the total amp-turns, which maps to the amount of conductor required, we take the integral of the norm of the current density. This is expressed as

$$At_{\text{ell}} = a \int_0^{2\pi} \left| \sum_{n=1}^{n_{\text{max}}} j_{0zn} \cos(n\psi) \right| d\psi, \quad (24)$$

for the elliptic current sheet, and as

$$At_{\text{cyl}} = r_0 \int_0^{2\pi} \left| \sum_{n=1}^{n_{\text{max}}} j_{0zn} \cos(n\theta) \right| d\theta, \quad (25)$$

for the circular sheet.

Table II shows these expressions evaluated for the dipole and quadrupole harmonics (using the methods previously developed in Sec. II to determine the elliptic current density coefficients which produce the circular harmonics). In the final two columns, the ratio of the stored energy and amp-turns between the elliptic and circular case is rewritten in terms of the ellipticity. Figures 5 and 6 illustrate these trends. For dipole magnets, the reduction in stored energy and amp-turns linearly approaches a factor of 2. For quadrupole magnets, the reduction is nonlinear, with the reduction in stored energy approaching a factor of 8 and the reduction in amp-turns approaching a factor of 4. These results quantify the advantages of choosing an elliptic aperture when possible and point to the increased benefits for higher order harmonics.

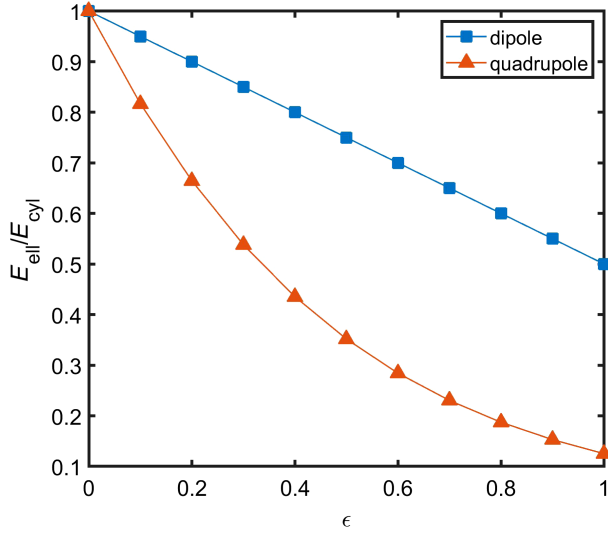


FIG. 5. Stored energy as a function of ellipticity normalized to the circular,  $\epsilon = 0$  case (see Fig. 4).

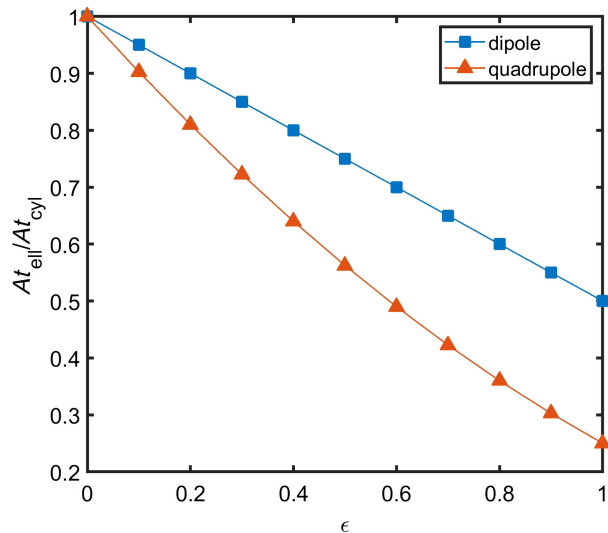


FIG. 6. Total amp-turns as a function of ellipticity normalized to the circular,  $\epsilon = 0$  case (see Fig. 4).

#### IV. APPLICATION TO CCT MAGNETS

In Sec. II, we developed an analytic approach relating the desired circular harmonics in an elliptic aperture to the current density on the elliptic surface. Now we focus on methods to approximate this idealized current density with discrete canted cosine theta (CCT) windings.

##### A. Averaging a CCT winding layer into a current sheet density

We begin the definition of an elliptic CCT winding layer by considering a parametric path constrained to the surface of an elliptic cylinder as illustrated in Fig. 7. We parametrize the position of this path in terms of the azimuthal angle as

$$\mathbf{p}(\psi) = a \cosh \eta_0 \cos \psi \hat{\mathbf{x}} + a \sinh \eta_0 \sin \psi \hat{\mathbf{y}} + p_z(\psi) \hat{\mathbf{z}}, \quad (26)$$

where  $\eta_0$  is the constant coordinate surface of the elliptic cylinder,  $\psi$  is the azimuthal angle, and  $p_z(\psi)$  is a yet

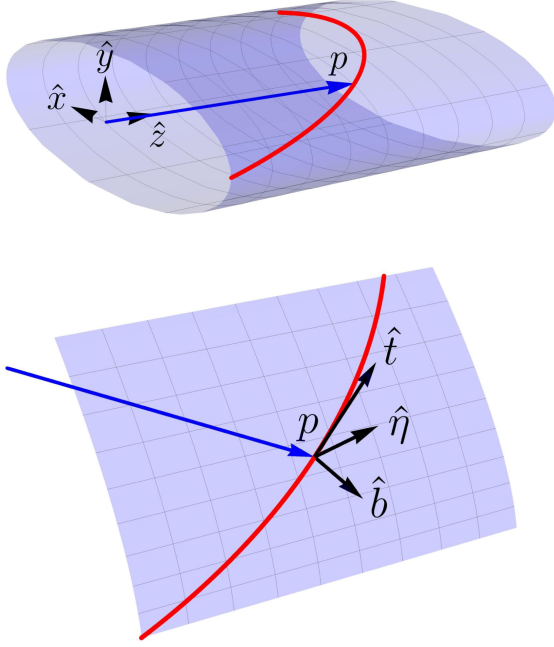


FIG. 7. The local unit tangent, radial, and binormal vectors ( $\hat{t}$ ,  $\hat{\eta}$ ,  $\hat{b}$ ) at point  $p$  of a parametric winding path constrained to the surface of an elliptic cylinder.

undefined function that describes the axial movement of the path. We define a local reference frame at location  $p(\psi)$  with  $\hat{t}$  tangential to the path,  $\hat{\eta}$  normal to the surface of the ellipse, and  $\hat{b}$  completing the orthogonal system (see Fig. 7). Vectors in these directions are

$$\mathbf{t}(\psi) = \frac{d\mathbf{p}}{d\psi} = h_2(\eta_0, \psi)\hat{\psi} + p'_z(\psi)\hat{z}, \quad (27)$$

and

$$\mathbf{b}(\psi) = \mathbf{t} \times \hat{\eta} = p'_z(\psi)\hat{\psi} - h_2(\eta_0, \psi)\hat{z}, \quad (28)$$

where the scale factor  $h_2$  is previously defined in Eq. (2).

From Eqs. (26)–(28), we see the choice of the axial position function  $p_z(\psi)$  is sufficient to define both the path and all local coordinate frame directions. As shown in Fig. 8, we assume the axial periodicity of the path to create

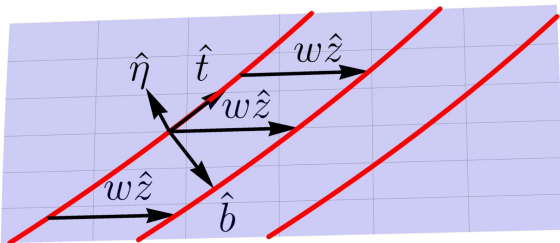


FIG. 8. We assume the winding path is axially periodic with pitch length  $w$ .

a uniform region away from the start and ends of coil. We require the axial distance between adjacent turns of the winding to be independent of  $\psi$ , meaning  $|p_z(\psi + 2\pi) - p_z(\psi)| = w$ , where the pitch  $w$  is the constant axial distance between turns (Fig. 8). With these assumptions, the approximate perpendicular distance between adjacent paths  $\delta(\psi)$  (in the direction of  $\hat{b}$ ) is

$$\delta(\psi) = w\hat{z} \cdot \hat{b} = \frac{wh_2(\eta_0, \psi)}{\sqrt{(p'_z(\psi))^2 + h_2(\eta_0, \psi)^2}}. \quad (29)$$

We assume the path  $p(\psi)$  represents a continuous line current of magnitude  $I_0$  and use the perpendicular spacing in Eq. (29) to average the winding path into an elliptic sheet current density of

$$\mathbf{j}(\psi) = \frac{I_0}{w} \left( \hat{\psi} + \frac{p'_z(\psi)}{a\sqrt{\cosh^2\eta_0 - \cos^2\psi}}\hat{z} \right). \quad (30)$$

This consists of two components: a constant azimuthal current (generating solenoidal fields) dependent on the pitch and an axial current varying with azimuthal angle (generating transverse fields) determined by  $p'_z(\psi)$ .

### B. Relating the winding path to magnetic field harmonics

We connect the CCT winding path to the field harmonics it produces through the choice of the axial path function  $p_z(\psi)$ . We look to find the form of  $p_z(\psi)$  so that the average sheet current density matches that derived from the elliptic harmonics in Sec. II (allowing the use of previously derived current-to-field relations for a continuous elliptic current sheet). From Eqs. (12) and (30), we see

$$\frac{I_0}{aw} \frac{p'_z(\psi)}{\sqrt{\cosh^2\eta_0 - \cos^2\psi}} = \frac{j_{0nz} \cos n\psi}{\sqrt{\cosh^2\eta_0 - \cos^2\psi}}, \quad (31)$$

which allows for finding the matching form of  $p_z(\psi)$  through the simple integration step

$$p_z(\psi) = \int \left( \frac{wa j_{0nz} \cos n\psi}{I_0} \right) d\psi. \quad (32)$$

With this, we write the axial path function in terms of the desired elliptic sheet current density coefficients  $j_{0nz}$  as

$$p_z(\psi) = \frac{wa j_{0nz}}{I_0} \frac{\sin n\psi}{n} + \frac{w}{2\pi}\psi, \quad (33)$$

where the extra term  $\frac{w}{2\pi}\psi$  is added to fulfill the condition of a continuous path with axial periodicity of pitch length  $w$ . Equation (33) combined with the definition of the parametric path in Eq. (26), using the parametric variable

TABLE III. Elliptic CCT winding path and field relation for producing the circular harmonics.

Desired	CCT axial path $p_z(\psi)$	$B_n$ (e.g., T/m $^{n-1}$ )
$B_1$	$\frac{a \sinh \eta_0}{\tan \alpha} \sin \psi$	$-\frac{\mu_0 I_0 \sinh \eta_0}{w \tan \alpha e^{\eta_0}}$
$B_2$	$\frac{a \sinh \eta_0}{2 \tan \alpha} \sin 2\psi$	$-\frac{2\mu_0 I_0 \sinh \eta_0}{aw \tan \alpha e^{2\eta_0}}$
$B_3$	$\frac{a \sinh \eta_0}{\tan \alpha} \left( \frac{1}{e^{2\eta_0}} \sin \psi + \frac{\sin 3\psi}{3} \right)$	$-\frac{4\mu_0 I_0 \sinh \eta_0}{a^2 w \tan \alpha e^{3\eta_0}}$
$B_4$	$\frac{a \sinh \eta_0}{\tan \alpha} \left( \frac{2}{e^{2\eta_0}} \frac{\sin 2\psi}{2} + \frac{\sin 4\psi}{4} \right)$	$-\frac{8\mu_0 I_0 \sinh \eta_0}{a^3 w \tan \alpha e^{4\eta_0}}$

$0 \leq \psi \leq 2\pi n_t$ , can be used to draw a continuous CCT winding path with  $n_t$  turns generating the desired elliptic harmonics far from the end effects of the windings.

The parameters defining a CCT layer with fixed elliptic aperture  $\eta_0$  are the wire current  $I_0$ , the axial pitch  $w$ , and the set of desired sheet current density coefficients  $j_{0nz}$ . For magnet design, it is advantageous to replace the current density coefficients with physical properties of the path itself (to decouple the powering current from the winding parameters). We do this by defining the midplane tilt angle  $\alpha$  of the winding path as

$$\tan(\alpha) = \frac{\mathbf{t} \cdot \hat{\boldsymbol{\psi}}}{\mathbf{t} \cdot \hat{\mathbf{z}}}\bigg|_{\psi=0} = \frac{I_0 \sinh \eta_0}{w j_{0nz}}, \quad (34)$$

assuming that the pitch  $w$  is much smaller than the ellipse focal length  $a$ . In this case, we rewrite the axial path function as

$$p_z(\psi) = \frac{a \sinh \eta_0}{n \tan \alpha} \sin n\psi + \frac{w}{2\pi} \psi, \quad (35)$$

which leads to an approximate sheet current density of

$$\mathbf{j}(\psi) = \frac{I_0}{w} \left( \hat{\boldsymbol{\psi}} + \frac{\frac{\sinh \eta_0}{\tan \alpha} \cos n\psi + \frac{w}{2\pi a}}{\sqrt{\cosh^2 \eta_0 - \cos^2 \psi}} \hat{\mathbf{z}} \right), \quad (36)$$

that is now dependent on geometric winding parameters. Here we see a single CCT winding layer contains three distinct currents: a constant azimuthal current which generates a solenoidal field inside the winding, a  $\cos(n\psi)$ -like axial current which produces transverse elliptic harmonics, and a pitch generated current axial current which maps to a constant  $n = 0$  component (generating fields outside the winding). The nonharmonic fields are derived in the Appendix.

### C. Circular field harmonics for elliptic CCT layers

We combine the method for relating the circular field harmonics to an elliptic current density from Sec. II with the derivation of the CCT path and current density in Eqs. (35) and (36) to determine the circular harmonics produced by a single CCT layer. For harmonics that only

require a single current density term (dipole and quadrupole), we simply relate the winding path and current density coefficients through

$$j_{0nz} = \frac{I_0 \sinh \eta_0}{w \tan \alpha}. \quad (37)$$

For combined function or higher order circular harmonics, which require a combination of  $j_{0nz}$  terms, the winding path coefficients must be weighted by the ratio of the desired current density terms. For these cases, special attention should be given to the physical meaning of the tilt angle  $\alpha$  due to multiple  $j_{0nz}$  terms contributing in Eq. (34).

Table III shares the CCT winding path and transfer function for the first four circular harmonics. Here we see the extra  $n - 2$  terms from the  $n \geq 3$  elliptic current sheet solution propagating through to the axial modulation of the winding path. Figure 9 shows an example winding layer with ellipticity of 0.6 for each of the harmonics in the table. In addition to a full layer with ends, this figure highlights the periodic symmetry region of axial pitch length  $w$  over which the winding turns are averaged into a sheet current density.

### D. Multilayer CCT magnet design

The average current density of a CCT layer in Eq. (36) contains two components that do not contribute to the desired harmonics. In the Appendix, we derive the fields produced by these components using integral methods. Similar to circular aperture CCT magnets, the constant azimuthal current produces a constant solenoidal field in the aperture and the pitch-generated axial current produces fields only in the region outside the winding.

For multilayer CCT magnets, we focus on an approach in which the undesirable solenoidal fields in the aperture cancel and the desired harmonic fields sum. We write the current density of the  $i$ th CCT layer located at the elliptic cylindrical surface  $\eta_{0i}$  as

$$\mathbf{j}_i(\psi) = \frac{I_{0i}}{w_i} \left( \hat{\boldsymbol{\psi}} + \frac{\frac{\sinh \eta_{0i}}{\tan \alpha_i} \cos n\psi + \frac{w_i}{2\pi a_i}}{\sqrt{\cosh^2 \eta_{0i} - \cos^2 \psi}} \hat{\mathbf{z}} \right). \quad (38)$$

For a total of  $n_{\text{lay}}$  layers, the solenoidal field in the aperture (from the Appendix) is

$$B_z = \mu_0 \sum_{i=1}^{n_{\text{lay}}} \frac{I_{0i}}{w_i}, \quad (39)$$

and polarity of the contribution of each layer to the transverse harmonics is given by the sign of  $I_{0i}/\tan \alpha_i$ .

With this, we see the approach of alternating the sign of the tilt angle  $\alpha$  and current  $I_0$  between an even number of layers nulls the undesired solenoidal field in the aperture

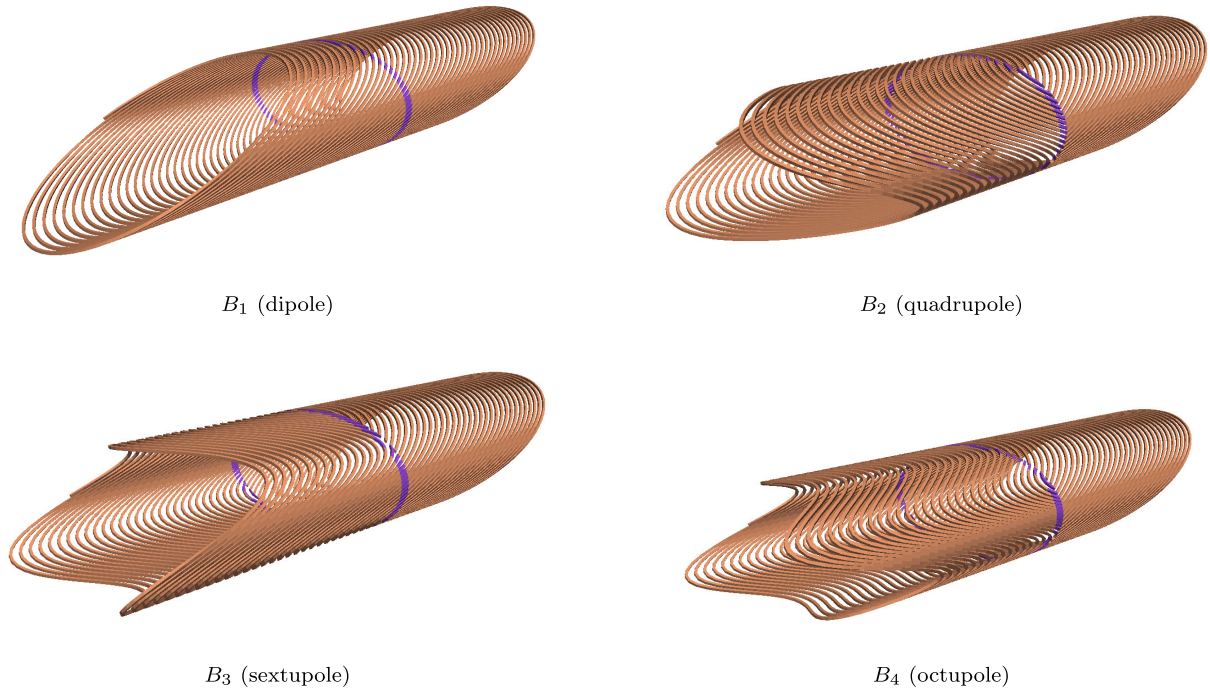


FIG. 9. Single layer elliptic CCT windings producing the first four circular harmonics (from Table III).

while leaving the polarity of the transverse harmonics unchanged (with the assumption of the same winding pitch  $w$ ). Figure 10 illustrates this approach for a pair of elliptic dipole layers. The alternation of the current  $I_0$  between layers has the additional benefit of bringing the current of a layer pair back to the same axial side of the magnet, simplifying the lead design.

**E. Discussion of CCT model assumptions**

While there are few limiting assumptions to the application of the current sheet density results in Sec. II, the analytic methods for CCT layer design include the important assumptions of (i) sufficient discrete turn density being averaged into a continuous current sheet and (ii) radially thin winding layers. For a given aperture, the first consideration is related to pitch of the winding  $w$ . In practice, this

is determined by  $w = (a_w + \delta) / \sin(\alpha)$ , where  $a_w$  is the width of the conductor channel (typically 1–2 mm for superconducting wires and cables),  $\delta$  is the midplane turn spacing (typically a metal rib of  $\approx 0.4$  mm), and  $\alpha$  is the midplane tilt angle (typically 15–25 degrees). From the author’s experience, the density resulting from these parameters typically leads to accelerator field quality ( $< 10^{-4}$  field errors) for dipole and quadrupole layers with an aperture larger than 50 mm.

This means we can typically design single wire, low-current CCT layers with a pure analytic approach. For high current designs, the use of a Rutherford cable requires further consideration of the orientation of the cable with respect to the elliptical surface and the field quality effects that come from no longer having a thin winding. In this case, a final numerical optimization of the winding parameters is likely required where the analytic case provides a starting point for optimization. This final step is not expected to be any more challenging than the similar approach being used to design high current CCT layers with circular aperture.

**V. CONCLUSION**

This work presented a framework for the analytic design of elliptic bore superconducting magnets. We started generally, by deriving the elliptic field harmonics and their relation to current density on an elliptic cylinder. Then, we shared the transformation between the elliptic and circular field harmonics, allowing for determining the elliptically shaped current density that produces the circular harmonics

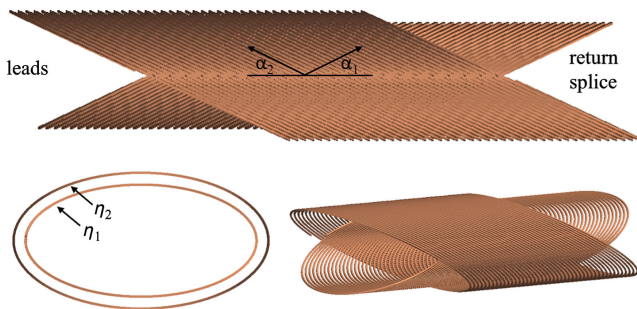


FIG. 10. An elliptic CCT dipole magnet with alternation of tilt angle and current direction between layers to cancel the solenoidal field in the aperture.

used in traditional accelerator design. With this, we explored the scaling of magnet cost parameters as a function of aperture ellipticity to quantify the advantages of choosing an elliptic bore for applications where the beam-prescribed field region is noncircular. Finally, we applied this general approach to the specific winding geometry of canted-cosine-theta (CCT) magnets, providing an analytic path to realistic coil designs for elliptic bore accelerator magnets.

Ultimately, the methodology we developed enables the determination of the superconducting winding geometry to produce a desired set of circular harmonics in an elliptic aperture—providing a full analytic path to the electromagnetic design of elliptic bore magnets. The next step toward demonstrating the technology is the design, fabrication, and test of a prototype elliptic bore CCT magnet. This effort benefits from the recent focus on the CCT design within the U.S. Magnet Development Program [22,23]. We plan to leverage the modular approach to circular bore CCT layer fabrication and magnet assembly established by this program to build and test a prototype elliptic bore magnet over the next several years.

### ACKNOWLEDGMENTS

The author acknowledges Dejan Trbojevic of Brookhaven National Laboratory for relating the importance of exploring elliptic bore superconductor magnets for fixed-field accelerators. In addition, he acknowledges the extensive analytic work of Shlomo Caspi for circular aperture magnets which provided an existing framework for how to approach the problem. Finally, he thanks LBNL colleagues D. Arbelaez, S. Caspi, P. Ferracin, J. L. Rudeiros Fernandez, and Y. Yang for feedback on this work and interesting discussions on the topic of elliptic bore magnets. This work was supported through the Early Career

Research Program by the Office of Science, Office of High Energy Physics, of the U.S. Department of Energy under Contract No. DE-AC02-05CH11231.

### APPENDIX: FINDING THE MAGNETIC VECTOR POTENTIAL IN ELLIPTIC COORDINATES WITH INTEGRATION TECHNIQUES

In Sec. II, we solved Laplace's equation in elliptic coordinates to find the magnetic vector potential and sheet current density producing 2D elliptic harmonics. With a known current density, we may take an alternative approach based on integration techniques. In this Appendix, we use this integral method to find the vector potential and fields from the sheet current density that approximates a CCT winding layer. Critically, we derive the solenoidal field produced by the azimuthal current density—a field component key to the design of CCT magnets which is not captured by the previous solution of Laplace's equation.

#### 1. Setting up the integration in elliptic coordinates

We use integration to find the magnetic vector potential from a sheet current density by adapting the approach shared by Caspi in Ref. [24] to elliptic cylindrical coordinates. If the primed coordinate  $\mathbf{r}'$  represents the location of source current  $\mathbf{J}$ , we find the magnetic vector potential  $\mathbf{A}$  at location  $\mathbf{r}$  using the integral form of Biot-Savart's law

$$\mathbf{A}(\mathbf{r}) = \frac{\mu_0}{4\pi} \int \frac{\mathbf{J}(\mathbf{r}')}{|\mathbf{r} - \mathbf{r}'|} d^3\mathbf{r}'. \quad (\text{A1})$$

If the source current is a sheet current density  $\mathbf{j}(\eta', \psi')$  located at the fixed elliptical boundary  $\eta' = \eta_0$ , the integral in elliptic coordinates is

$$\mathbf{A}(\mathbf{r}) = \frac{\mu_0}{4\pi} \int_0^{2\pi} \int_{-\infty}^{\infty} \int_0^{\infty} \frac{\mathbf{j}(\eta', \psi') \delta(\eta' - \eta_0)}{|\mathbf{r} - \mathbf{r}'|} h_{\eta'} h_{\psi'} h_z d\eta' dz' d\psi', \quad (\text{A2})$$

where the scale factors are given in Eq. (2). Evaluating the  $\eta'$  integral and substituting the remaining scale factors leads to

$$\mathbf{A}(\mathbf{r}) = \frac{a\mu_0}{4\pi} \int_0^{2\pi} \mathbf{j}(\eta_0, \psi') \sqrt{\cosh^2 \eta_0 - \cos^2 \psi'} \int_{-\infty}^{\infty} \frac{1}{|\mathbf{r} - \mathbf{r}'|} dz' d\psi'. \quad (\text{A3})$$

To prepare for integration, we manipulate the equation for the distance between source and field points in elliptic coordinates into the form

$$|\mathbf{r} - \mathbf{r}'| = \sqrt{\frac{a^2 e^{2\eta_0}}{4} (1 - 2e^{(\eta-\eta_0)} \cos(\psi - \psi') + e^{2(\eta-\eta_0)}) (1 - 2e^{-(\eta+\eta_0)} \cos(\psi + \psi') + e^{-2(\eta+\eta_0)}) + (z - z')^2}. \quad (\text{A4})$$

A step-by-step process to reaching this form is in the Supplemental Material [25]. Next, we introduce the integration variable  $s = z - z'$  and perform the axial integration step

$$\int_{-\infty}^{\infty} \frac{1}{|\mathbf{r} - \mathbf{r}'|} dz' = \int_{-\infty}^{\infty} \frac{1}{\sqrt{C_1 + s^2}} ds = -2 \ln(\sqrt{C_1}), \quad (\text{A5})$$

where non- $s$  dependent terms in Eq. (A4) are grouped into  $C_1$  and constants are omitted. This leads to a form of

$$-2 \ln(\sqrt{C_1}) = -\ln\left(\frac{a^2 e^{2\eta_0}}{4}\right) - \ln(1 - 2e^{(\eta-\eta_0)} \cos(\psi - \psi') + e^{2(\eta-\eta_0)}) - \ln(1 - 2e^{-(\eta+\eta_0)} \cos(\psi + \psi') + e^{-2(\eta+\eta_0)}). \quad (\text{A6})$$

We use the general identity

$$\ln(1 - 2x \cos \phi + x^2) = -2 \sum_{k=1}^{\infty} \frac{\cos k\phi}{k} x^k \quad |x| \leq 1 \quad (\text{A7})$$

from Ref. [26] to rewrite Eq. (A6) as

$$-2 \ln(\sqrt{C_1}) = \begin{cases} -\ln\left(\frac{a^2 e^{2\eta_0}}{4}\right) + 2 \sum_{k=1}^{\infty} \frac{\cos k(\psi - \psi')}{k} \left(\frac{e^\eta}{e^{\eta_0}}\right)^k + 2 \sum_{k=1}^{\infty} \frac{\cos k(\psi + \psi')}{k} \left(\frac{e^{-\eta}}{e^{\eta_0}}\right)^k, & \eta < \eta_0 \\ -\ln\left(\frac{a^2 e^{2\eta}}{4}\right) + 2 \sum_{k=1}^{\infty} \frac{\cos k(\psi - \psi')}{k} \left(\frac{e^{\eta_0}}{e^\eta}\right)^k + 2 \sum_{k=1}^{\infty} \frac{\cos k(\psi + \psi')}{k} \left(\frac{e^{-\eta}}{e^{\eta_0}}\right)^k, & \eta > \eta_0 \end{cases}, \quad (\text{A8})$$

where for regions outside the sheet,  $\eta \geq \eta_0$ , we factor out  $e^{2(\eta-\eta_0)}$  to maintain the conditions in Eq. (A7) identity. We will use this form of  $-2 \ln(\sqrt{C_1})$  in the azimuthal integral equation

$$\mathbf{A}(\mathbf{r}) = \frac{a\mu_0}{4\pi} \int_0^{2\pi} \mathbf{j}(\eta_0, \psi') \sqrt{\cosh^2 \eta_0 - \cos^2 \psi'} \left(-2 \ln(\sqrt{C_1})\right) d\psi' \quad (\text{A9})$$

to find the magnetic vector potential produced by each of the three current density components in a CCT layer.

## 2. Vector potential for the $\cos n\psi$ -like current producing the elliptic harmonics

In Sec. II, we derived the elliptic harmonics by solving the vector Laplace equation. It is good practice to verify that the integral approach reproduces this result. To prepare for integration, we rewrite the current density from Eq. (12) as

$$\mathbf{j} = j_{0nz} \frac{\cos(n\psi) \cos(nt) + \sin(n\psi) \sin(nt)}{\sqrt{\cosh^2 \eta_0 - \cos^2 \psi'}} \hat{\mathbf{z}} \quad (\text{A10})$$

to include the integration variable  $t = \psi - \psi'$  (for which the form also matches  $t = \psi + \psi'$ ). We combine this with Eqs. (A8) and (A9) to set up the vector potential integral as

$$\mathbf{A}(\mathbf{r}) = \frac{a\mu_0 j_{0nz}}{4\pi} \int_0^{2\pi} [\cos(n\psi) \cos(nt) + \sin(n\psi) \sin(nt)] \hat{\mathbf{z}} \begin{cases} -\ln\left(\frac{a^2 e^{2\eta_0}}{4}\right) + 2 \sum_{k=1}^{\infty} \frac{\cos kt}{k} \left(\frac{e^{k\eta} + e^{-k\eta}}{e^{k\eta_0}}\right) dt, & \eta < \eta_0 \\ -\ln\left(\frac{a^2 e^{2\eta}}{4}\right) + 2 \sum_{k=1}^{\infty} \frac{\cos kt}{k} \left(\frac{e^{k\eta_0} + e^{-k\eta_0}}{e^{k\eta}}\right) dt, & \eta > \eta_0 \end{cases}. \quad (\text{A11})$$

The inner product of the trigonometric functions results in the integral picking out only the  $n = k$  terms, leading to a potential of

$$\mathbf{A}(\mathbf{r}) = \frac{a\mu_0 j_{0nz} \cos n\psi}{n} \begin{cases} e^{-n\eta_0} \cosh(n\eta) \hat{\mathbf{z}}, & \eta < \eta_0 \\ e^{-n\eta} \cosh(n\eta_0) \hat{\mathbf{z}}, & \eta > \eta_0 \end{cases}, \quad (\text{A12})$$

where we use the identity  $\cosh(nx) = (e^{nx} + e^{-nx})/2$  for further simplification. As expected, this result exactly matches the vector potential derived from Laplace's equation in Eq. (13) for the elliptic harmonics.

## 3. Vector potential for the constant azimuthal current producing solenoidal fields

We see from Eq. (36) that a CCT winding layer generates a constant azimuthal current density  $\mathbf{j} = \frac{I_0}{w} \hat{\boldsymbol{\psi}}'$ . To prepare for integration, we first rewrite the direction  $\hat{\boldsymbol{\psi}}'$  in terms of  $\hat{\boldsymbol{\eta}}$  and  $\hat{\boldsymbol{\psi}}$ . Then we reformat this result in the integration variables

$\psi - \psi'$  and  $\psi + \psi'$  to match the form of Eq. (A8). After much manipulation, shown step-by-step in the Supplemental Material [25], this results in

$$\begin{aligned} \mathbf{j} = & \frac{I_0}{w} \hat{\psi}' = \frac{I_0}{w} \frac{1}{\sqrt{\cosh^2 \eta - \cos^2 \psi} \sqrt{\cosh^2 \eta_0 - \cos^2 \psi'}} \\ & \times (\cos(\psi - \psi') [\cosh(\eta) \sinh(\eta_0) \sin(\psi) \cos(\psi) - \sinh(\eta) \cosh(\eta_0) \sin(\psi) \cos(\psi)] \hat{\boldsymbol{\eta}} \\ & + \cos(\psi - \psi') [\sinh(\eta) \sinh(\eta_0) \cos^2(\psi) + \cosh(\eta) \cosh(\eta_0) \sin^2(\psi)] \hat{\boldsymbol{\psi}} \\ & + \cos(\psi + \psi') [\sinh(\eta) \cosh(\eta_0) \sin(\psi) \cos(\psi) + \cosh(\eta) \sinh(\eta_0) \sin(\psi) \cos(\psi)] \hat{\boldsymbol{\eta}} \\ & + \cos(\psi + \psi') [\sinh(\eta) \sinh(\eta_0) \cos^2(\psi) - \cosh(\eta) \cosh(\eta_0) \sin^2(\psi)] \hat{\boldsymbol{\psi}} \\ & + \sin(\psi - \psi') \text{ and } \sin(\psi + \psi') \text{ terms)} \end{aligned} \quad (\text{A13})$$

where only the  $\cos(\psi - \psi')$  and  $\cos(\psi + \psi')$  terms that contribute to integration are shown. This form of the current is combined with Eqs. (A8) and (A9) and integrated to find the potential. This picks out the  $k = 1$  terms only and leads to a potential of

$$\mathbf{A}(\mathbf{r}) = \frac{a\mu_0 I_0}{2w} \frac{1}{\sqrt{\cosh^2 \eta - \cos^2 \psi}} \left[ \left( -\frac{1}{4} e^{-2(\eta+\eta_0)} - \frac{1}{4} e^{4\eta-2(\eta+\eta_0)} + \frac{1}{2} \right) \sin(2\psi) \hat{\boldsymbol{\eta}} + \frac{1}{4} (e^{4\eta} - 1) e^{-2(\eta+\eta_0)} [e^{2\eta_0} - \cos(2\psi)] \hat{\boldsymbol{\psi}} \right] \quad (\text{A14})$$

inside the windings ( $\eta \leq \eta_0$ ). We find the magnetic field with

$$\mathbf{B}(\mathbf{r}) = \nabla \times \mathbf{A} = \frac{\hat{\mathbf{z}}}{a(\cosh^2 \eta - \cos^2 \psi)} \left[ \frac{\partial}{\partial \eta} \left( \sqrt{\cosh^2 \eta - \cos^2 \psi} A_\psi \right) - \frac{\partial}{\partial \psi} \left( \sqrt{\cosh^2 \eta - \cos^2 \psi} A_\eta \right) \right], \quad (\text{A15})$$

resulting in a constant solenoidal field inside the aperture of strength

$$\mathbf{B}(\mathbf{r}) = \frac{\mu_0 I_0}{w} \hat{\mathbf{z}}. \quad (\text{A16})$$

#### 4. Vector potential for the nonharmonic axial current producing azimuthal fields outside the layer

From Eq. (36), we see the CCT winding creates a pseudoconstant axial current density

$$\mathbf{j} = \frac{I_0}{2\pi a \sqrt{\cosh^2 \eta_0 - \cos^2 \psi'}} \hat{\mathbf{z}}, \quad (\text{A17})$$

which is combined with Eqs. (A8) and (A9) to set up the integration as

$$\mathbf{A}(\mathbf{r}) = \frac{a\mu_0 I_0}{4\pi} \frac{1}{2\pi a} \int_0^{2\pi} \hat{\mathbf{z}} \begin{cases} -\ln\left(\frac{a^2 e^{2\eta_0}}{4}\right) + 2 \sum_{k=1}^{\infty} \frac{\cos kt}{k} \left(\frac{e^{k\eta} + e^{-k\eta}}{e^{k\eta_0}}\right) dt, & \eta < \eta_0 \\ -\ln\left(\frac{a^2 e^{2\eta}}{4}\right) + 2 \sum_{k=1}^{\infty} \frac{\cos kt}{k} \left(\frac{e^{k\eta_0} + e^{-k\eta_0}}{e^{k\eta}}\right) dt, & \eta > \eta_0 \end{cases}. \quad (\text{A18})$$

The potential resulting from this integral is

$$\mathbf{A}(\mathbf{r}) = \frac{\mu_0 I_0}{4\pi} \begin{cases} -\ln\left(\frac{a^2 e^{2\eta_0}}{4}\right) \hat{\mathbf{z}}, & \eta < \eta_0 \\ -\ln\left(\frac{a^2 e^{2\eta}}{4}\right) \hat{\mathbf{z}}, & \eta > \eta_0 \end{cases}, \quad (\text{A19})$$

$$\mathbf{B}(\mathbf{r}) = \nabla \times \mathbf{A} = \frac{1}{a \sqrt{\cosh^2 \eta - \cos^2 \psi}} \left( \frac{\partial A_z}{\partial \psi} \hat{\boldsymbol{\eta}} - \frac{\partial A_z}{\partial \eta} \hat{\boldsymbol{\psi}} \right) \quad (\text{A20})$$

evaluate to

$$\mathbf{B}(\mathbf{r}) = \frac{\mu_0 I_0}{4\pi} \frac{1}{a \sqrt{\cosh^2 \eta - \cos^2 \psi}} \begin{cases} 0, & \eta < \eta_0 \\ 2\hat{\boldsymbol{\psi}}, & \eta > \eta_0 \end{cases}. \quad (\text{A21})$$

from which the fields

This current density component (which is generated by the forward pitch of the windings) is not typically relevant for CCT magnet design since it does contribute to fields in the aperture.

- 
- [1] S. Machida *et al.*, Acceleration in the linear non-scaling fixed-field alternating-gradient accelerator EMMA, *Nat. Phys.* **8**, 243 (2012).
- [2] A. Bartnik *et al.*, CBETA: First multipass superconducting linear accelerator with energy recovery, *Phys. Rev. Lett.* **125**, 044803 (2020).
- [3] Y. Iwata *et al.*, Design of a compact superconducting accelerator for advanced heavy-ion therapy, *Nucl. Instrum. Methods Phys. Res., Sect. A* **1053**, 168312 (2023).
- [4] A. Mierau, E. Fischer, F. Kaether, C. Roux, A. Bleile, V. Marusov, K. Sugita, P. Szwangruber, H. Weiss, H. Khodzhbagiyani, and S. Kostromin, Testing of the superconducting magnets for the SIS100 synchrotron, *IEEE Trans. Appl. Supercond.* **28**, 1 (2018).
- [5] P. Spiller *et al.*, The FAIR Heavy Ion Synchrotron SIS100, *J. Instrum.* **15**, T12013 (2020).
- [6] M. L. Lopes, V. Kashikhin, J. C. Tompkins, and A. V. Zlobin, Design studies of a dipole with elliptical aperture for the Muon Collider Storage Ring, in *Proceedings of the 3rd International Particle Accelerator Conference, New Orleans, LA, 2012* (IEEE, Piscataway, NJ, 2012).
- [7] N. Mokhov, V. Kashikhin, S. Striganov, I. Tropin, and A. Zlobin, The Higgs Factory muon collider superconducting magnets and their protection against beam decay radiation, *J. Instrum.* **13**, P10024 (2018).
- [8] T. Obana, T. Ogitsu, T. Nakamoto, K. Sasaki, A. Yamamoto, T. Oriyasa, M. Yoshimoto, and Y. Mori, Magnetic field design of a superconducting magnet for a FFAG accelerator, *IEEE Trans. Appl. Supercond.* **15**, 1185 (2005).
- [9] K. Mizushima, Y. Yang, T. Fujimoto, Y. Iwata, S. Matsuba, Y. Abe, E. Noda, M. Urata, T. Shirai, T. Oriyasa, S. Takayama, S. Amano, K. Nakanishi, and Y. Hirata, Concept design of a superconducting magnet for a Compact Heavy-Ion Synchrotron, *IEEE Trans. Appl. Supercond.* **32**, 1 (2022).
- [10] Y. Yang, S. Matsuba, K. Mizushima, T. Fujimoto, Y. Iwata, E. Noda, M. Urata, T. Shirai, G. Nishijima, S. Takayama, S. Amano, T. Maeto, T. Oriyasa, K. Nakanishi, and Y. Hirata, Design and test of a 0.4-m long short model of a conduction-cooled superconducting combined function magnet for a compact, rapid-cycling heavy-ion synchrotron, *Nucl. Instrum. Methods Phys. Res., Sect. A* **1050**, 168165 (2023).
- [11] A. Portone, W. Baker, E. Salpietro, A. Vostner, P. Bruzzone, F. Cau, A. Della Corte, A. Di Zenobio, E. Theisen, A. Baldini, P. Testoni, J. Lucas, M. Pinilla, and G. Samuelli, Design and procurement of the European Dipole (EDIPO) superconducting magnet, *IEEE Trans. Appl. Supercond.* **18**, 499 (2008).
- [12] P. Bruzzone, L. Bottura, F. Cau, G. De Rijk, P. Ferracin, J. Minervini, A. Portone, S. Prestemon, E. Rochepault, E. Ravaioli, G. Sabbi, and P. Testoni, *IEEE Trans. Appl. Supercond.* **28**, 1 (2018).
- [13] J. L. R. Fernandez, D. Arbelaez, P. Ferracin, R. Hafalia, R. Lee, P. Mallon, S. Prestemon, G. Sabbi, T. Tristan, and G. Vallone, Engineering design of a large aperture 15 T Cable Test Facility dipole magnet, *IEEE Trans. Appl. Supercond.* **32**, 1 (2022).
- [14] P. Schnizer, *Advanced Multipoles for Accelerator Magnets* (Springer, New York, 2017).
- [15] B. Auchmann, S. Kurz, C. Petrone, and S. Russenschuck, Generalized harmonic analysis of computed and measured magnetic fields, *IEEE Trans. Magn.* **52**, 1 (2016).
- [16] D. Meyer and R. Flasck, A new configuration for a dipole magnet for use in high energy physics applications, *Nucl. Instrum. Methods* **80**, 339 (1970).
- [17] C. Goodzeit, R. Meinke, and M. Ball, Combined function magnets using double-helix coils, in *Proceedings of the 22nd Particle Accelerator Conference, PAC-2007, Albuquerque, NM* (IEEE, Albuquerque, NM, 2007), pp. 560–562.
- [18] S. Caspi, F. Borgnolutti, L. Brouwer, D. Cheng, D. R. Dietderich, H. Felice, A. Godeke, R. Hafalia, M. Martchevskii, S. Prestemon, E. Rochepault, C. Swenson, and X. Wang, Canted-cosine-theta magnet (CCT)—a concept for high field accelerator magnets, *IEEE Trans. Appl. Supercond.* **24**, 1 (2014).
- [19] P. Moon and D. Spencer, *Field Theory Handbook* (Springer-Verlag, Berlin, 1961).
- [20] P. Moon and D. Spencer, The meaning of the vector Laplacian, *J. Franklin Inst.* **256**, 551 (1953).
- [21] M. Green and B. Strauss, The cost of superconducting magnets as a function of stored energy and design magnetic induction times the field volume, *IEEE Trans. Appl. Supercond.* **18**, 248 (2008).
- [22] S. Prestemon, K. Amm, L. Cooley, S. Gourlay, D. Larbalestier, G. Velev, and A. Zlobin, The 2020 updated roadmaps for the US magnet development program, [arXiv:2011.09539](https://arxiv.org/abs/2011.09539).
- [23] D. Arbelaez *et al.*, Status of the Nb3Sn canted-cosine-theta dipole magnet program at Lawrence Berkeley National Laboratory, *IEEE Trans. Appl. Supercond.* **32**, 1 (2022).
- [24] S. Caspi, The vector potential and stored energy of thin cosine (n theta) helical wiggler magnet, LBL Public Report No. 38075, 1995.
- [25] See Supplemental Material at <http://link.aps.org/supplemental/10.1103/PhysRevAccelBeams.27.022402> for additional steps in the process to find the vector potential by integration.
- [26] I. Gradshteyn and I. Ryzhik, *Table of Integrals, Series and Products* (Elsevier, New York, 2007).